biomechanics

Article

Application of the Strain Energy Density Criterion for Patient-Specific Geometry-Based Fracture Healing Simulation

Tingyu Dai [1], Robin Reinardt [1], Michael Roland [1], Stefan Diebels [1], Bergita Ganse [2], Marcel Orth [3] and Gargi Shankar Nayak [1,4,5,*]

[1] Chair of Applied Mechanics, Saarland University, Campus A4 2, 66123 Saarbruecken, Germany; tingyu.dai@uni-saarland.de (T.D.); robin.reinardt@uni-saarland.de (R.R.); m.roland@mx.uni-saarland.de (M.R.); s.diebels@mx.uni-saarland.de (S.D.)
[2] Innovative Implant Development (Fracture Healing), Saarland University, Kirrberger Str. 1, bld. 57, 66421 Homburg, Germany; bergita.ganse@uks.eu
[3] Department of Trauma, Hand and Reconstructive Surgery, Departments and Institutes of Surgery, Saarland University, 66421 Homburg, Germany; marcel.orth@uks.eu
[4] Bio-Mechanics & Materials Group, Department of Head and Neck Medicine, University Medical Center of the Johannes Gutenberg University Mainz, 55131 Mainz, Germany
[5] Platform for Biomaterial Research, BiomaTiCS Group, University Medical Center of the Johannes Gutenberg University Mainz, 55131 Mainz, Germany
* Correspondence: gargi.nayak@uni-mainz.de

Abstract

Background/Objectives: Strain energy density-based algorithms are widely applied in modelling bone healing, yet their use under patient-specific geometry-based conditions remains underdeveloped. This study proposes a patient-specific geometry-based framework for fracture healing simulation and investigates how different postoperative loading conditions influence the mechanical environment of callus remodeling. **Methods**: Using postoperative radiographic data of a 63-year-old male patient with a distal diaphyseal tibial fracture and concomitant proximal and distal fibular fractures, a three-dimensional finite element model of the tibia was reconstructed, imported into a multiphysics simulation environment, and coupled with an iterative numerical algorithm. A uniform initial callus density of 750 kg/m^3 was assumed as a simplified and homogenized representation of the healing tissue. The effects of different mechanical loading conditions (partial weight-bearing, physiological loading, and supraphysiological loading) on the mechanical response and density evolution of the callus were evaluated. **Results**: Partial weight-bearing resulted in insufficient mechanical stimulation and progressive density loss within the callus. Physiological loading generated strain energy density levels consistent with known osteogenic ranges and contributed to continuous cortical shell formation and overall density increase. Supraphysiological loading was associated with overload-related resorption and spatial heterogeneity, which may reduce callus stability. **Conclusions**: The findings suggest that loading magnitude may influence the simulated remodeling response of the callus under the assumptions of the present model. These results indicate that intermediate loading conditions were associated with a more pronounced remodeling response compared to reduced or excessive loading for the investigated case. The comparison with postoperative clinical imaging showed qualitative agreement in the spatial distribution of mineralized and less mineralized regions, supporting the feasibility of the proposed patient-specific geometry-based SED-based framework.

Keywords: strain energy density; bone remodeling; digital medicine; fracture healing

Academic Editor: Fan Gao and Sujata Khandare

Received: 23 March 2026
Revised: 5 May 2026
Accepted: 7 May 2026
Published: 11 May 2026

1. Introduction

Despite advancements in medical technology, fracture non-union remains a significant clinical challenge. Fracture non-union is generally defined as a fracture that fails to unite within at least six months after the initial injury or shows no visible progression toward healing over a three-month period [1]. For instance, tibial fractures exhibit a non-union rate of approximately 14% [2]. Non-union incurs high socioeconomic costs [3], and it can lead to limitations in ambulation, chronic pain, reduced ability to participate in occupational and social activities, and a diminished health-related quality of life [4].

However, addressing these issues is demanding, as effective fracture treatment requires considering biomechanical (fracture stability) and biological factors alike [5]. Attempting full weight-bearing with inadequate fractured bone strength may inhibit and prolong the healing process [6]. Conversely, inadequate mechanical loading likewise has a negative influence and may delay the healing process [7]. Thus, investigating how different loading conditions influence fracture healing is of great interest for clinicians. At present, recommendations regarding the type and dose of weight-bearing activity after lower limb fractures are still largely based on empirical evidence rather than reproducible biomechanical data, partly because the mechanical environment that supports bone healing remains insufficiently characterized [8]. Although patients cannot precisely control the loads transmitted through the injured limb during daily activities [9,10], such information is increasingly relevant for the design and evaluation of emerging smart implants with active actuation capabilities. These implant concepts rely on a detailed understanding of load-dependent healing stimuli to adaptively modulate the mechanical environment around the fracture [11].

One of the most influential concepts for describing the relationship between mechanical loading and bone adaptation is Frost's Mechanostat theory [12]. This theory states that specific mechanical strain thresholds, which are tissue-specific, govern bone adaptation; different skeletal structural tissues, such as cortical bone, trabecular bone, cartilage, and ligaments, have distinct threshold values due to their biological and mechanical properties. Strains below the lower threshold (disuse window) trigger bone resorption and reduce bone mass; strains within the intermediate range (adapted or lazy zone) maintain bone mass and architecture with minimal remodeling; strains above the upper modeling threshold stimulate bone formation, increasing strength and mass; and strains beyond the pathological overload threshold cause microdamage, triggering repair-related remodeling [12]. This threshold-based concept guides the definition of loading conditions that facilitate bone healing and prevent damage from excessive strain. On tissue level, mechanosignalling [13] is key for these tissue adaptation processes.

Over the past decades, simulation technologies have attracted increasing attention as innovative tools in fracture treatment research [14–17]. Generally, mechanobiological models based on tissue differentiation theories are used to model the initial bone healing phase, whereas strain energy density (SED)-based models are applied to model the bone remodeling process [18–24]. However, in the recent past Celik et al. developed a computational framework using SED as a key parameter to model bone remodeling around dental implants during the healing period [22]. While this study demonstrated the utility of SED as a mechanobiological stimulus and provided insights into long-term bone density changes under cyclic loading, its scope was limited to idealized, non-patient-specific geometry-based scenarios. Such simplifications restrict their applicability to real-world clinical cases where variability in patient anatomy, weight-bearing conditions, implant positioning and tissue properties significantly influence the fracture healing scenario.

The present study addresses these gaps by proposing a patient-specific, geometry-based finite element framework for simulating SED-driven callus remodeling. By integrat-

https://doi.org/10.3390/biomechanics6020046

ing clinical imaging data, model-defined loading conditions, and an iterative remodeling algorithm, the framework enables the investigation of load-dependent remodeling behaviour in a clinically derived fracture scenario.

2. Materials and Methods

2.1. SED-Based Bone Remodeling Algorithm

In this study, bone remodeling within the fracture callus was described using a strain energy density (SED)-based algorithm. The mechanical stimulus was defined as the SED per unit apparent density (U/ρ), where U represents the local strain energy density and ρ denotes the apparent density. This formulation accounts for the site-specific mechanical environment within the callus and enables normalization of the mechanical stimulus with respect to local tissue properties.

The temporal evolution of density was governed by the remodeling law proposed by Li et al. [25], expressed as:

$$\frac{d\rho}{dt} = \begin{cases} 0, & if\, \frac{u}{\rho} \epsilon [(1-w)k, (1+w)k] \\ B\left(\frac{U}{\rho} - k\right) - D\left(\frac{U}{\rho} - k\right)^2, & otherwise \end{cases} \tag{1}$$

where k is the reference mechanical stimulus defining the homeostatic state, and w represents the width of the "lazy zone," within which no remodeling occurs. Outside this range, the balance between bone formation and resorption is controlled by the parameters B and D, which regulate the rate and nonlinearity of density adaptation. In the present study, w was set to 0.2, B to 1.0 (g·cm^{-3})^2·MPa^{-1}·(time unit)$^{-1}$, and D to 60 (g·cm^{-3})^2·MPa^{-2}·(time unit)$^{-1}$. The parameter k was calibrated to 0.0004 J/g to represent the mechanical sensitivity of mineralizing callus tissue. It should be noted that k is not treated as a universal constant, but rather as a tissue-dependent parameter reflecting the current state of callus maturation.

To link density evolution with mechanical properties, the Young's modulus (E) was related to apparent density via an empirical power-law relationship [26]:

$$E(\rho) = C\rho^3 \tag{2}$$

where C = 3790 MPa·(g·cm^{-3})$^{-3}$ is a material constant. This relationship enables continuous updating of material stiffness during the remodeling process.

Based on the resulting Young's modulus, the tissue within the callus was categorized into different structural states: regions with $E < 5$ GPa were considered non-mineralized tissue, regions with 5–16 GPa were classified as trabecular bone, and regions with 16–20 GPa were defined as cortical bone [27–29]. This classification provides a qualitative interpretation of the spatial progression of callus mineralization during remodeling.

2.2. Patient-Specific Geometry-Based Model Development

This study investigated the case reported by Orth et al. of a 63-year-old male, height 180 cm and weight 95 kg, who sustained fractures of the tibia and the proximal as well as distal end of the fibula [30]. The patient underwent an initial closed reduction stabilized with an external fixator, followed by intramedullary nailing of the tibia and plate osteosynthesis of the distal fibular fracture. This study focused on analysing the sensitivity of callus remodeling in a patient who, after six weeks postoperative with approximately 35% body weight (BW) loading, was subsequently allowed to progress to full weight-bearing as recommended by the surgeon. A 3D tibial model was reconstructed from CT data using Synopsys Simpleware™ software, version 2024.06 (Synopsys, Inc., Sunnyvale, CA, USA), a specialized platform for converting medical imaging datasets into high-quality computational models. Semi-automatic segmentation was performed to distinguish cortical bone, trabecular bone, orthopedic implants, and fracture gaps, followed by manual refinement together with the treating surgeon to ensure anatomical accuracy. The study focused exclusively on the tibia and the fracture callus, excluding the fibula from the analysis. The segmented 3D reconstruction is shown in Figure 1, where the tibia is depicted in grey, the fracture callus in red, and the orthopedic implants and screws in brown. Although the full tibial geometry was included in the FE model to ensure realistic load transfer, only the callus region was considered for the evaluation of material properties in the simulations.

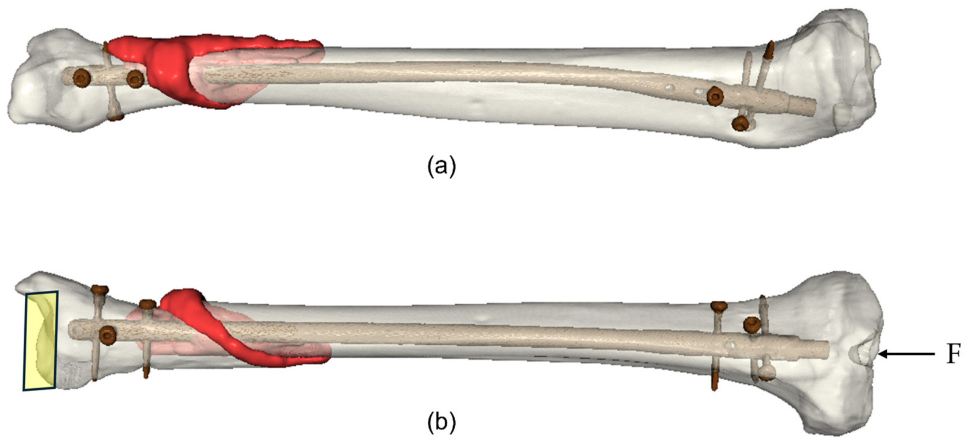

Figure 1. Segmented 3D reconstruction of the post-operative tibial model. (**a**) Medial–lateral view of the tibia. (**b**) Anterior–posterior view of the tibia.

A high-resolution FE mesh was generated using quadratic tetrahedral elements, comprising 79,218 elements for the implant, 41,766 for the callus, and 244,072 for the bone, thereby balancing computational efficiency and numerical accuracy. The selected mesh density follows previously established workflows reported in the literature [30], in which high-resolution image-based FE models were used to simulate fracture mechanics and bone healing. Accordingly, the adopted mesh is considered sufficiently refined to capture the relevant mechanical response. Cortical and trabecular bone were differentiated using a grey value threshold derived from the CT data. Based on this classification, material properties were assigned to assuming linear elastic, isotropic behavior. Cortical bone was assigned a Young's modulus of 18 GPa and a Poisson's ratio of 0.30, while trabecular bone was assigned a Young's modulus of 7.5 GPa and a Poisson's ratio of 0.30. The initial callus was assigned a density of 750 kg/m^3 and a Young's modulus of 1.6 GPa. The selected Young's modulus values fall within the range reported in the literature for cortical and trabecular bone [27–29]. The orthopedic implant and screws were modeled as titanium alloy with a Young's modulus of 108 GPa and a Poisson's ratio of 0.37, consistent with previously reported material properties of Ti-based implants [18].

The meshed model was imported into COMSOL Multiphysics® software, version 6.3 (COMSOL AB, Stockholm, Sweden), where boundary conditions and physiological loading were defined. Boundary conditions were defined to represent physiological load transfer during gait. The distal end of the tibia was fully constrained in all translational and rotational degrees of freedom, representing the mechanical support provided by the ankle joint. At the proximal tibia, external forces were applied to simulate joint contact loading during walking. The load was decomposed into three orthogonal components (X, Y, Z), corresponding to the medial–lateral, anterior–posterior, and distal–proximal directions, respectively, as illustrated in Figure 1b. This loading configuration was derived from in vivo measurements reported in the Orthoload database [31,32], which provides knee joint contact forces during level walking. In this dataset, the peak knee joint contact force reached approximately −251% BW along the z-axis, while the forces along the x- and y-axes were considerably smaller (0.2% and 0.3% BW, respectively). These force magnitudes reflect the combined effects of ground reaction forces and muscle actions during normal gait. In this study, the peak resultant force from Orthoload was defined as the physiological reference load, and the applied loading scenarios (35%, 100%, and 200%) were expressed as percentages of this reference load. Here, 35% served as partial weight-bearing, 100% corresponded to physiological loading during normal walking, and 200% represented supraphysiological overloading. The x-, y-, and z-directions were assigned to the medial–lateral, anterior–posterior, and distal–proximal axes of the tibia, respectively. The z-directional peak corresponds to the moment when the contralateral leg lifts off during gait, whereas characteristic x- and y-directional peaks occur near foot flat, heel strike, and toe-off.

For the FE analysis, the axial load at contralateral leg lift-off, together with its corresponding x- and y-components, was applied to the proximal tibia. The simulated callus was subsequently loaded with 35%, 100%, and 200% of the physiological reference load to investigate its remodeling response under reduced, physiological, and elevated loading conditions. Each simulation was iterated for 300 remodeling steps. The simulations were performed solely on the tibial 3D model. As the fibula contributes to load sharing, its omission may slightly overestimate the mechanical demand borne by the tibia.

An iterative MATLAB R2025a algorithm (MathWorks, Natick, MA, USA), implemented via COMSOL LiveLink™ for MATLAB, automated the simulation by updating density-dependent material properties of the callus, recalculating SED distributions, and repeating the FE analysis until convergence.

2.3. Numerical Implementation and Workflow

The numerical implementation of the remodeling algorithm was performed using a coupled FE and MATLAB framework. The overall workflow is illustrated in Figure 2. The simulations were conducted in an iterative manner, in which the apparent density and corresponding material properties of the callus were updated based on the local mechanical stimulus. At each iteration step, an FE analysis was carried out in COMSOL Multiphysics to compute the spatial distribution of SED within the callus under the applied loading conditions. The resulting SED values were then exported to MATLAB via LiveLink™, where the density update was calculated for each element according to the remodeling law described in Section 2.2. The updated density field was subsequently reassigned to the FE model, and the material properties were recalculated using the density–modulus relationship. This process was repeated iteratively until the prescribed number of remodeling steps was reached.

To ensure numerical stability and avoid non-physical behavior, constraints were imposed on the density update. The maximum allowable change in density per iteration was limited to 20 kg/m^3 to prevent abrupt variations. In addition, lower and upper bounds of 10 kg/m^3 and 1740 kg/m^3 were enforced, representing the range from soft tissue to fully mineralized cortical bone. These constraints ensured that the remodeling process remained within physiologically meaningful limits.

Each simulation was performed for 300 iterations, allowing the temporal evolution of density and material properties to be captured. The resulting spatial distribution of density and corresponding mechanical properties was used to evaluate the remodeling response of the callus under different loading conditions.

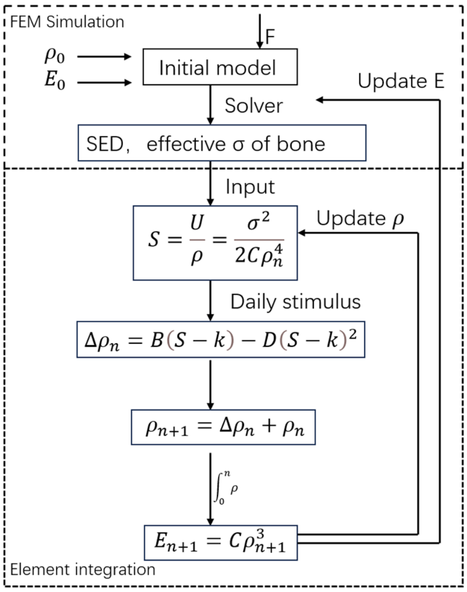

Figure 2. Outline of the callus remodeling algorithm used in FE model analysis, based on the methodology described in Hasan [15].

3. Results

Simulations under varying loading levels revealed pronounced differences in the SED distribution during callus remodeling after 300 interactions (Figure 3a–c). Following the classification algorithm proposed by J. Li et al. [25], the mechanical stimulus can be divided into four regions: underload resorption (red), lazy zone (blue), bone formation (green), and overload resorption (yellow).

Under the first loading cycle, the simulated callus exhibited SED ranges of 0.0004–36.8 J/kg under partial weight-bearing, 0.003–268 J/kg physiological loading, and 0.01–1075 J/kg under supraphysiological loading. As the applied load increased, both the minimum and maximum SED values rose by several orders of magnitude, indicating a clear load-dependent scaling of the mechanical stimulus within the callus. The SED range obtained under the physiological loading conditions agrees well with the FE bone remodeling model of Weinans et al. [33], which reported reference values of approximately 4 J/kg for the femoral shaft and 250 J/kg for an idealized cortical plate. This agreement suggests that the physiological loading condition provides a mechanically relevant stimulus for callus remodeling. In contrast, values under the partial weight-bearing condition are largely below the range reported in the literature, whereas those under supraphysiological loading substantially exceed it, both of which may be less conducive to consolidation under the assumptions of the present model.

To further elucidate the temporal evolution of the mechanical environment during callus remodeling, Figure 3d–f present the relative proportions of elements classified into the four Mechanostat regions over 300 iterations under different loading conditions. By comparing the proportions of bone formation, overload resorption, and underload resorption, a clear shift in dominance can be observed throughout the simulation. Across the three loading cases, clear differences were observed in the relative proportions of the four remodeling regions. Under partial weight bearing, underload resorption represented the largest proportion and increased from approximately 52.7% to 63.2%, while bone formation decreased from about 35.3% to 25.3%. The lazy zone remained around 10.4–10.9%, and overload resorption stayed low, decreasing from approximately 1.1% to 0.6%. Under full weight bearing, bone formation was the dominant proportion at the beginning, with values above 71%, but decreased gradually to approximately 57.6%. Underload resorption first decreased from about 14.3% to 9.0%, and then increased to approximately 23.1%, while the lazy zone increased from around 6.0% to 6.9%. Overload resorption increased initially to about 13.7% and then remained relatively stable around 12–13%. Under supraphysiological loading, the distribution was markedly different: overload resorption accounted for a much larger proportion, increasing from approximately 30.7% to above 44%, whereas underload resorption remained comparatively low, mostly between 3.0% and 5.8%. Bone formation decreased from approximately 63.7% to about 47.5%, and the lazy zone stayed at a low level, generally between 1.0% and 2.1%. Overall, the proportional distribution of remodeling regions differed clearly among the three loading cases, with partial weight bearing showing the highest underload resorption proportion, full weight bearing showing the highest bone formation proportion, and 200% weight bearing showing the highest overload resorption proportion.

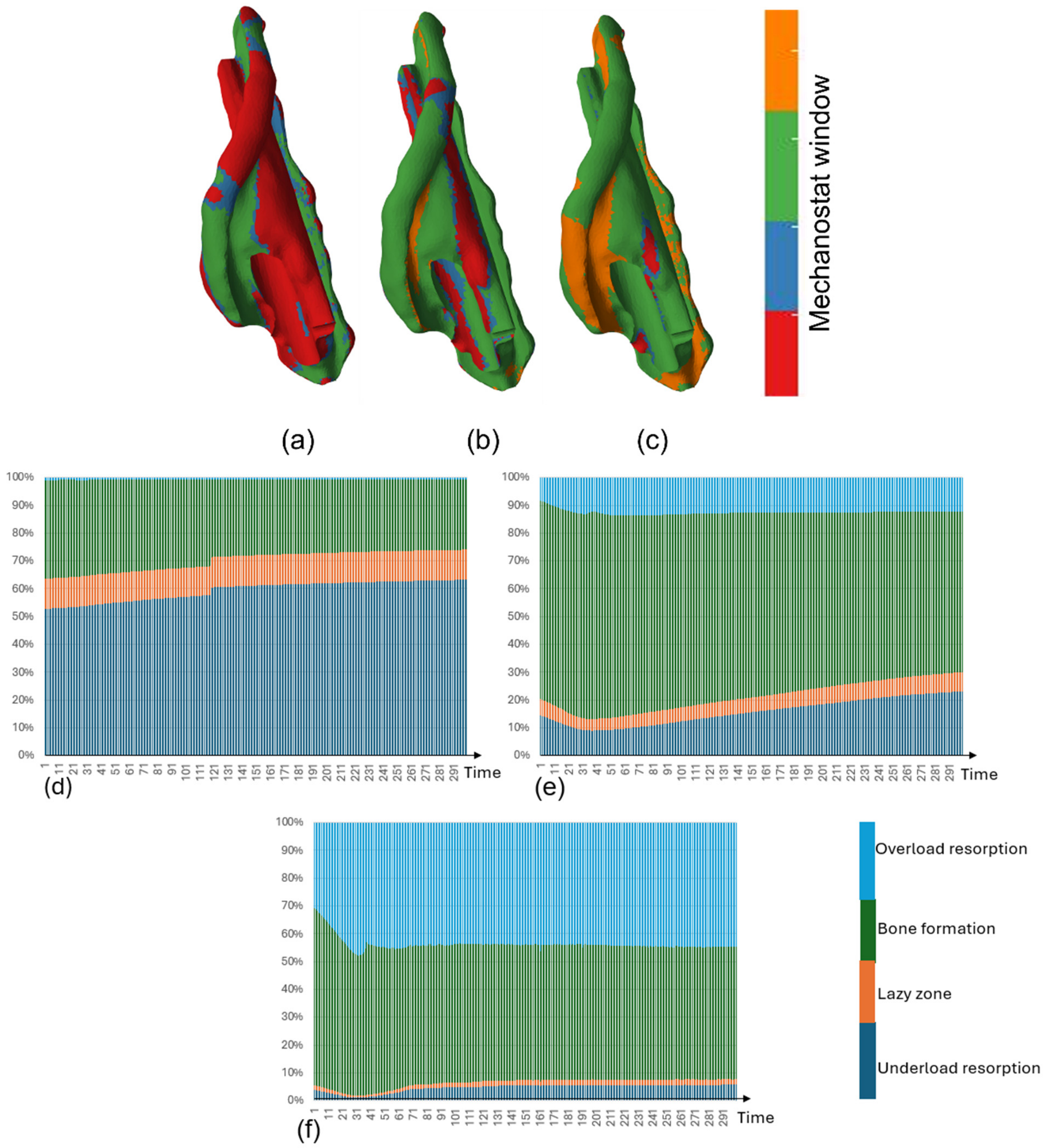

Figure 3. Distribution of SED within the callus after 300 interactions under (**a**) partial weight-bearing, (**b**) physiological loading, and (**c**) supraphysiological loading. Proportional distribution of the remodeling regions during the iteration process under different loading conditions: (**d**) partial weight bearing, (**e**) full weight bearing, and (**f**) supraphysiological loading. The stacked bars show the relative proportions of underload resorption, lazy zone, bone formation, and overload resorption.

These findings suggest that the simulated callus exhibits a distinct load-dependent response. The physiological loading condition was associated with a comparatively more consistent mechanical environment within the present model, whereas both partial weight-bearing and supraphysiological loading shifted many elements outside the favorable range of the Mechanostat window, thereby adversely affecting the remodeling process.

Based on the SED-driven remodeling algorithm, the callus density evolution was closely associated with variations in the SED distribution. When the modeled callus was subjected to partial weight-bearing, the density gradually decreased throughout the remodeling process. After 300 remodeling iterations, a widespread reduction in density (red regions) was observed, as shown in Figure 4a. In contrast, when the applied load was increased to physiological loading, the callus density exhibited a clear upward trend, with extensive regions of density gain (green areas), suggesting a more pronounced remodeling response, as illustrated in Figure 4b. However, under supraphysiological loading, most regions once again demonstrated a sharp decline in density, reflecting overload-induced resorption, as shown in Figure 4c.

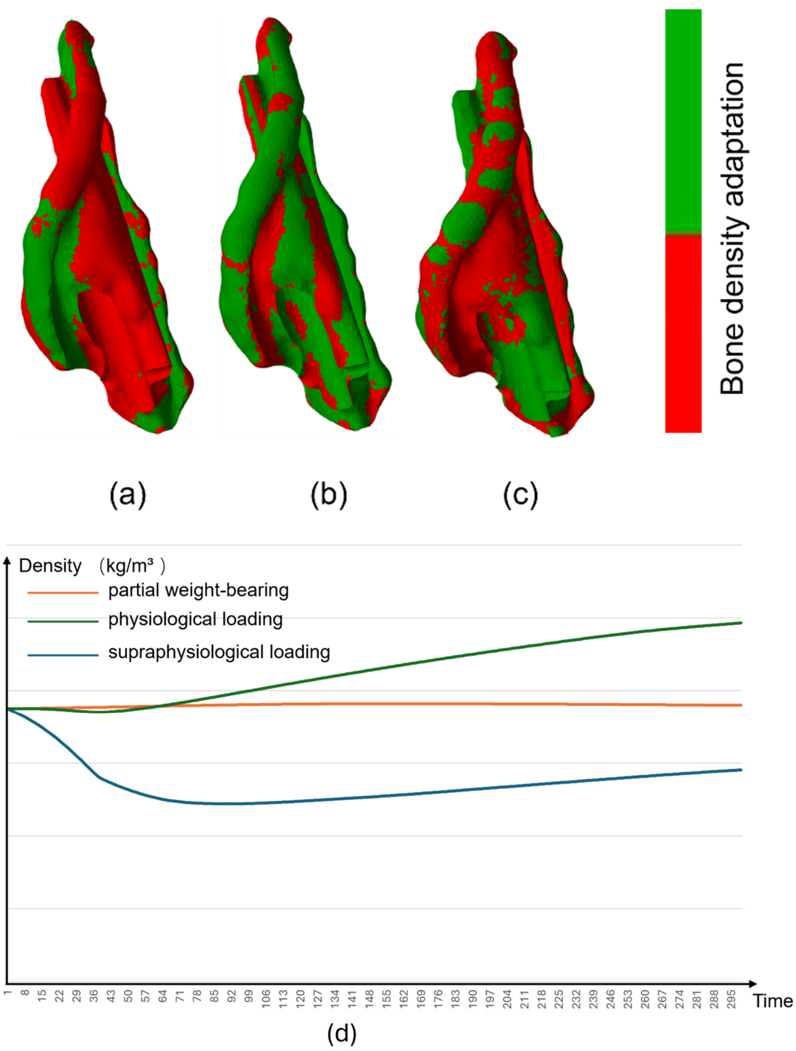

Figure 4. Distribution of callus density after 300 remodeling iterations under different loading conditions: (**a**) partial weight-bearing, (**b**) physiological loading, and (**c**) supraphysiological loading. Green regions represent bone formation associated with adequate mechanical stimulation, whereas red regions indicate density loss caused by either insufficient loading or overload-induced resorption. (**d**) Evolution of the average density under different loading conditions.

The temporal evolution of the average density, as shown in Figure 4d, exhibits distinct responses under the three loading conditions. Under partial weight-bearing, the density remains relatively stable, varying only within a narrow range between approximately 750.0 and 764.1 kg/m^3 throughout the simulation. In contrast, under physiological loading, the density shows a slight initial decrease from 750.0 to approximately 740.5 kg/m^3, followed by a continuous increase, reaching about 986.2 kg/m^3 at the end of the simulation, which is the highest among all cases. Under supraphysiological loading, the density decreases sharply during the early iterations from 750.0 to a minimum value of approximately 488.1 kg/m^3 and subsequently recovers gradually to around 581.1 kg/m^3. However, it remains significantly lower than the other two cases at the final stage.

As shown in Figure 5a–c, cortical bone gradually formed under both physiological loading and supraphysiological loading; however, the spatial distribution of newly formed cortical bone differed between the two cases.

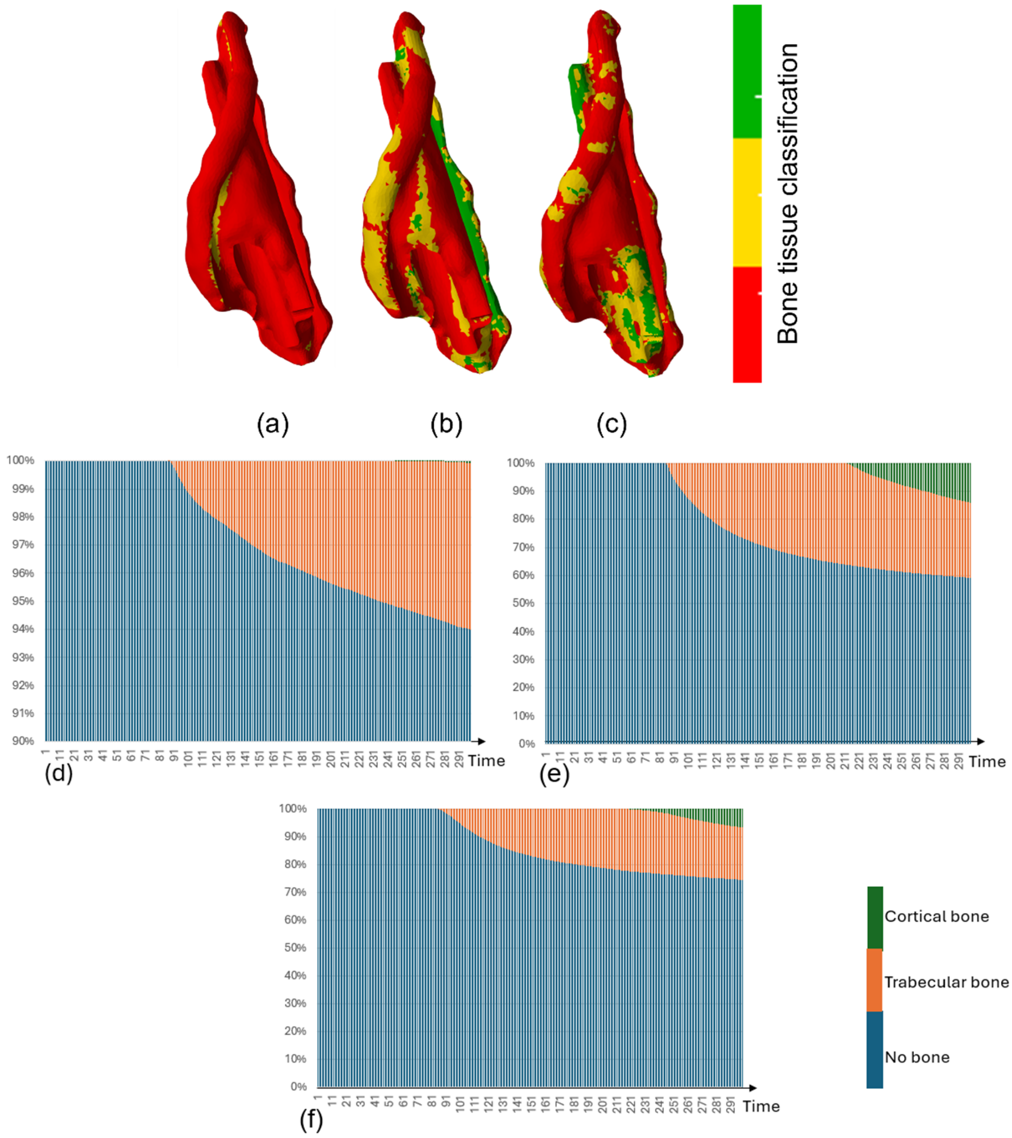

Figure 5. Distribution of tissue types within the callus after 300 remodeling iterations under different loading conditions: (**a**) partial weight-bearing, (**b**) physiological loading, and (**c**) supraphysiological loading. Elements were classified according to Young's modulus thresholds: no bone (<5 GPa, red), trabecular bone (5–16 GPa, yellow), and cortical bone (16–20 GPa, green) [27–29]. Temporal evolution of tissue composition in the callus under different loading conditions: (**d**) partial weight-bearing, (**e**) physiological loading, and (**f**) supraphysiological loading.

Under reduced loading, the callus mainly consisted of low-density tissue, indicating that the mechanical stimulus was insufficient to induce ossification. Under physiological loading, a continuous cortical layer and a well-developed trabecular network were formed, suggesting that the tissue had progressed to a more advanced stage of maturation. Under supraphysiological loading, the callus exhibited pronounced spatial heterogeneity, with discontinuous and fragmented cortical structures that failed to provide adequate mechanical stability to the construct.

As shown in Figure 5d–f, the distribution of tissue types differed markedly among the three loading conditions. Under 35% partial weight-bearing, the callus remained dominated by low-stiffness tissue, which decreased only slightly from 100% initially to approximately 94.0% at the final stage. In contrast, trabecular bone increased gradually to about 5.9%, while cortical bone remained negligible, accounting for less than 0.1%. Under physiological loading, the proportion of low-stiffness tissue decreased more substantially to approximately 59.2%, accompanied by a pronounced increase in trabecular and cortical bone fractions to about 26.8% and 14.1%, respectively. Under supraphysiological loading, the final distribution consisted of approximately 74.5% low-stiffness tissue, 18.8% trabecular bone, and 6.7% cortical bone. Overall, physiological loading resulted in the highest proportion of mature bone tissue, whereas partial weight-bearing led to minimal cortical bone formation.

To better visualize the distribution of bone tissue around the fracture fragments, the callus was sectioned along the medial–lateral and anterior–posterior planes, and the results were compared with the postoperative X-ray images obtained seven months postoperatively. Figure 6b shows the slice of the initial callus with a uniform Young's modulus of 1.6 GPa. Figure 6c depicts the same region after 300 remodeling iterations under physiological loading, where the tissue classification reveals the differentiation of the callus into trabecular and cortical bone. The figure provides a magnified view of the region (in red) shown in Figure 6b, illustrating local mineralization and tissue maturation along the fracture margins.

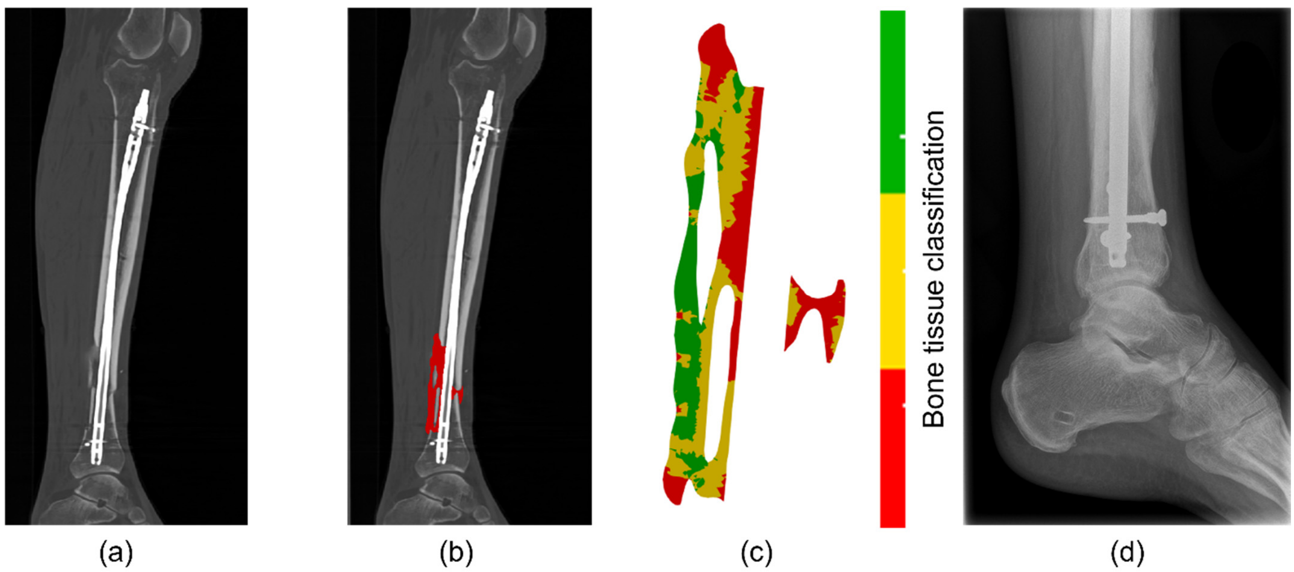

Figure 6. Comparison between clinical imaging and simulation results from the medial–lateral view. (**a**,**b**) Postoperative CT scans of the tibia showing the fixation implant in place and the segmented callus region highlighted in red. (**c**) The result of FE simulation displaying lateral slices of the callus after 300 remodeling iterations under physiological loading, illustrating tissue classification where red, yellow, and green represent non-mineralized tissue, trabecular bone, and cortical bone, respectively. (**d**) Postoperative X-ray image demonstrating full weight-bearing with intramedullary nail fixation in situ.

https://doi.org/10.3390/biomechanics6020046

In the postoperative CT scan (Figure 6a), a clear interfragmentary gap can still be observed between the fracture fragments, indicating incomplete consolidation during the early healing phase. In contrast, the X-ray image obtained seven months after surgery (Figure 6d) shows complete posterior bridging of the fracture gap, while the anterior region remains partially filled with immature trabecular bone of relatively low radiodensity. This observation aligns closely with the simulation results, which also demonstrate asymmetrical bone formation—dense cortical bone forming along the posterior and outer cortical regions that connect the fragments, whereas in the anterior view, trabecular bone occupies a broad region, but cortical bone formation remains incomplete.

When examining the anterior–posterior view of the X-ray (Figure 7d), it becomes apparent that the outer regions protruding from the bone are not yet fully mineralized, and the fracture gap in this view is not filled with high-density bone. The simulation supports these findings (Figure 7c), showing low-density regions at the periphery and a fracture gap filled only with trabecular bone. This indicates that the model can reproduce plausible spatial patterns of callus remodeling, which may evolve toward the original bone shape over time. The qualitative agreement between the simulation results and postoperative imaging further suggests that the proposed framework can capture spatially heterogeneous healing patterns.

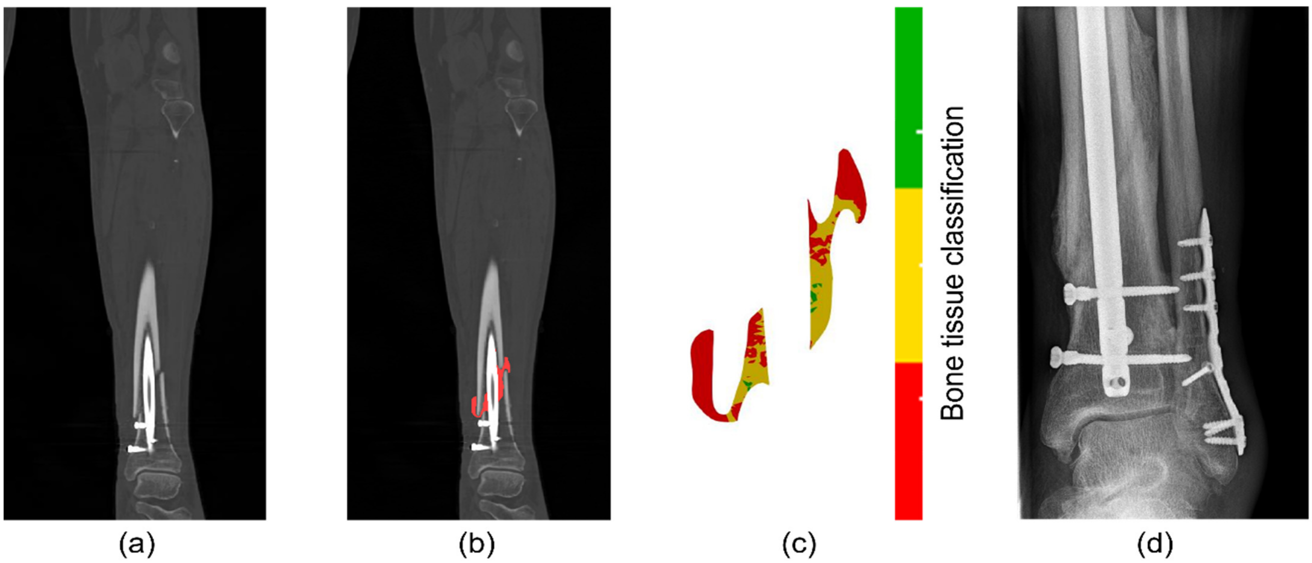

Figure 7. Comparison between clinical imaging and simulation results from the anterior–posterior view. (**a**,**b**) Postoperative CT scans showing the fixation implant and the segmented callus region highlighted in red. (**c**) The result of FE simulation displaying anterior–posterior slices of the callus after 300 remodeling iterations under physiological loading, illustrating tissue classification where red, yellow, and green represent non-mineralized tissue, trabecular bone, and cortical bone, respectively. (**d**) Postoperative X-ray image obtained seven months after surgery showing satisfactory bone healing with the fixation in place.

4. Discussion and Conclusions

This study proposed a patient-specific geometry-based FE framework for simulating SED-driven callus remodeling and explored its behavior under different postoperative loading conditions. The model is able to simulate adaptive responses of bone tissue under varying mechanical stimuli within the simplified mechanical assumptions adopted in this study, suggesting its potential to provide mechanistic insights into the impact of loading conditions on fracture healing. By integrating patient-specific anatomical geometry with literature-informed material properties assigned to cortical and trabecular bone as well as implants, together with mechanically defined loading conditions, the proposed framework provides a more clinically relevant representation of the fracture healing process. SED remains a central parameter, but its integration is enhanced by considering dynamic mechanical environments and heterogeneous callus states that reflect the variability in the modeled conditions.

The results demonstrated that callus remodeling is highly sensitive to external mechanical loading, consistent with previous mechanobiological findings showing that tissue differentiation and repair outcomes depend strongly on the timing and magnitude of mechanical stimulation during healing [34]. In the modeled callus, partial weight-bearing conditions provided insufficient mechanical stimulation to sustain bone formation, leading to a gradual reduction in density dominated by resorptive activity. Under physiological loading conditions, the SED distribution and density evolution were associated with a more consistent remodeling trend within the assumptions of the present model, characterized by the formation of a continuous cortical shell and increased structural consolidation. In contrast, supraphysiological loading was associated with overload-related resorption and spatial heterogeneity within the callus, which may be associated with a reduction in its overall mechanical stability.

The classification of tissue types further confirmed that appropriate mechanical loading promotes the transition of the callus from low-density tissue to mature cortical bone, whereas both insufficient and excessive loading impede ossification. The simulated spatial distribution of bone tissue showed qualitative agreement with the postoperative radiographs. This supports the feasibility of the framework and suggests that it can capture plausible spatial trends in this specific case.

Within the present framework, the cubic density–modulus relationship proposed by Carter et al. implies that the mass-specific mechanical stimulus scales with ρ^3 and ε^2. As callus density and stiffness increase, strain under a given load decreases, such that higher external forces are required to maintain the target SED. This mechanism helps explain the observed trend in the simulation, in which physiological loading was associated with a more pronounced remodeling response for the initial callus. In contrast, lower loading levels appeared insufficient for this stage and may be more relevant to a phase of healing that was not explicitly modeled in the present study. Although this finding is consistent with the clinical strategy of staged loading (dynamisation) and supported by experimental studies, its interpretation should remain within the assumptions of the present modeling framework. The result primarily reflects mechanical response characteristics under specific conditions, and its applicability to broader clinical scenarios requires further evaluation across multiple patients, fracture geometries, fixation constructs, and loading conditions. Gardner et al. applied cyclic axial compression to healing mouse tibiae and found that higher forces were needed at later healing stages to enhance callus stiffness, whereas Mehta et al. reported increased callus volume and mineralisation when semi-rigid fixation allowed greater interfragmentary motion in young, but not aged, rats [35,36]. Although neither study quantified SED directly, their outcomes suggest that the osteogenic load must increase as the regenerate stiffens.

The numerical SED values reported here remain contingent on the adopted density modulus law; alternative ρ-E relationships would shift the absolute window, but the relative state dependence should persist. Expressing results in both external and internal SED terms facilitates cross-study comparison and translation to fixation design. Putative biological modifiers such as age, vascularity and systemic disease were deliberately held constant in the present analysis and merit explicit inclusion in future work.

The loading conditions in this study were based on a single peak load derived from the Orthoload database and scaled to represent different weight-bearing scenarios. This simplified approach was intentionally adopted to enable a controlled comparison of load magnitude effects on the remodeling process. In reality, postoperative loading is more complex, involving cyclic variations, muscle forces, and patient-specific factors, which were not explicitly included. Therefore, the peak load was used as an approximation of the dominant mechanical stimulus driving callus remodeling.

It must be noted, however, that truly uniaxial compression is uncommon in vivo. Because the tibial shaft is gently curved, any small lateral offset of the joint reaction force generates an additional bending moment that places the anterior cortex in tension and the posterior cortex in compression. Cadaver experiments have shown that such bending can govern the failure location even when the external load is nominally axial [37]. This observation is consistent with material level data. Cortical bone is only about 10–30% stronger in compression than in tension, so tensile stresses on the convex side of the bent shaft often set the functional strength limit [38].

From a mechanobiological perspective, the optimal stimulus for fracture healing is therefore one of predominant axial compression coupled with low but not zero bending and shear. Experimental osteotomy models demonstrate that small cyclic axial micromotions ($\approx$1–3% gap strain) accelerate callus maturation, whereas large shear or bending amplitudes delay union [36,39]. Contemporary fixation systems accordingly aim to bias load transfer towards compression while constraining excessive rotation and flexure. The present findings, which isolate the osteogenic potency of pure z-axis loading, reinforce this design philosophy but also underscore the necessity to account for inevitable off-axis components when translating numerical predictions into clinical protocols.

In addition, all tissues were modeled as linear elastic materials, which is a simplification of the actual behavior of biological tissues. This assumption may affect the absolute values of the computed SED but is considered sufficient for comparing relative trends under different loading conditions.

However, while the SED-based model performs well in simulating mechanical adaptability, its simplified mechanical framework overlooks biological factors such as cellular activity and biochemical signals. To improve the model's accuracy, future research should incorporate biological processes (e.g., osteoblast proliferation, osteoclast activity, and further stem cell differentiation) into the framework. In addition, many non-union cases are caused by insufficiencies on the biological level, such as a diminished blood supply [3].

Moreover, the present model does not account for the concomitant double fracture of the fibula nor the osteosynthesis of its distal part, although this injury was present in the clinical case. This simplification may lead to a systematic overestimation of the mechanical load carried by the tibia, as load sharing between tibia and fibula is neglected. Consequently, the influence of mechanical stimuli on spatial healing patterns—such as asymmetric cortical bridging—may be misrepresented. This limitation should therefore be considered when interpreting the relationship between simulated loading conditions and the observed healing outcomes. Additionally, the mechanical contribution of skeletal muscles was not included in the simulation. Muscle forces are known to induce additional deformation modes, particularly torsional loading of the tibia during gait phases such as push-off [40,41]. Neglecting these contributions may reduce the accuracy of the predicted strain energy density distribution and its link to callus remodeling behavior.

Finally, the present study only used a single patient case for simulation to show technical feasibility. To derive generalizable findings of weight-bearing scenarios, that are generally valid for most patients, a group of patients with varying fracture types, sexes and age groups would need to be studied. Therefore, the results presented here may not be transferable to other patients. Furthermore, a limitation of this workflow is that it cannot be immediately applied in the daily clinical context due to its complexity. At present, the proposed framework should be interpreted as a research-oriented and proof-of-concept approach rather than a tool intended for routine clinical application.Automated software solutions would need to be developed to allow clinicians to actually use these simulations in their daily work. It is, however, a valuable asset for fracture healing research.

In summary, the results emphasize the importance of applying appropriate mechanical forces in bone healing and demonstrate the potential of SED-based models in deepening the understanding of callus remodeling. By combining patient-specific geometry-based data with advanced simulation techniques, the model provides a comprehensive perspective on the dynamic mechanisms underlying fracture healing. The findings aim to mitigate complications and improve the understanding of recovery processes for complex fractures. This study seeks to bridge the gap between theoretical simulations and their potential application in clinical practice by integrating patient-specific anatomical data with a mechanistic SED-based remodeling framework to investigate load-dependent callus adaptation in a clinically derived fracture scenario. However, further development is needed to integrate the biological complexities, which will pave the way for more accurate and comprehensive predictions of bone healing and treatment strategies.

Author Contributions: Formal analysis: T.D., G.S.N., M.R., S.D., R.R., B.G. and M.O.; Funding acquisition: B.G., S.D. and G.S.N.; Investigation: T.D.; Methodology: T.D., G.S.N., R.R. and M.R.; Supervision: G.S.N., M.R. and S.D.; Writing—original draft preparation: T.D.; Writing—review and editing: G.S.N., M.R., R.R., S.D., B.G. and M.O. All authors have read and agreed to the published version of the manuscript.

Funding: This study was partly funded by the Werner Siemens Foundation under the grant "Smart Implants 2.0".

Institutional Review Board Statement: Ethical approval was obtained from the IRB of Saarland Medical Board (Aerztekammer des Saarlandes, Germany, application number 30/21). Informed consent was obtained according to the Declaration of Helsinki. The study is part of the project Smart Implants 2.0-Weight-bearing and Gait Observation for Early Monitoring of Fracture Healing and Individualized Therapy after Trauma, funded by the Werner Siemens Foundation. It is registered in the German Clinical Trials Register (DRKS-ID: DRKS00025108).

Informed Consent Statement: Informed consent was obtained from all subjects involved in the study.

Data Availability Statement: Due to personal data protection laws, the datasets used in this study cannot be shared with external researchers.

Conflicts of Interest: The authors declare no conflicts of interest.

Abbreviations

The following abbreviations are used in this manuscript:

SED	Strain Energy Density
FE	Finite Element
FEM	Finite Element Method
CT	Computed Tomography
BW	Body Weight

References

1. Nicholson, J.A.; Makaram, N.; Simpson, A.; Keating, J.F. Fracture nonunion in long bones: A literature review of risk factors and surgical management. *Injury* **2021**, *52*, S3–S11. [CrossRef]
2. Zura, R.; Xiong, Z.; Einhorn, T.; Watson, J.T.; Ostrum, R.F.; Prayson, M.J.; De La Rocca, G.J.; Mehta, S.; McKinley, T.; Wang, Z.; et al. Epidemiology of fracture nonunion in 18 human bones. *JAMA Surg.* **2016**, *151*, e162775. [CrossRef] [PubMed]

3. Rupp, M.; Biehl, C.; Budak, M.; Thormann, U.; Heiss, C.; Alt, V. Diaphyseal long bone nonunions—Types, aetiology, economics, and treatment recommendations. *Int. Orthop.* **2018**, *42*, 247–258. [CrossRef] [PubMed]
4. Brinker, M.R.; Hanus, B.D.; Sen, M.; O'Connor, D.P. The devastating effects of tibial nonunion on health-related quality of life. *J. Bone Jt. Surg. Am.* **2013**, *95*, 2170–2176. [CrossRef] [PubMed]
5. Ulstrup, A.K. Biomechanical concepts of fracture healing in weight-bearing long bones. *Acta Orthop. Belg.* **2008**, *74*, 291–302.
6. Augat, P.; Merk, J.; Ignatius, A.; Margevicius, K.; Bauer, G.; Rosenbaum, D.; Claes, L. Early, full weight-bearing with flexible fixation delays fracture healing. *Clin. Orthop. Relat. Res.* **1996**, *328*, 194–202. [CrossRef]
7. Mavčič, B.; Antolič, V. Optimal mechanical environment of the healing bone fracture/osteotomy. *Int. Orthop.* **2012**, *36*, 689–695. [CrossRef]
8. Zhang, L.; Miramini, S.; Richardson, M.; Ebeling, P.; Little, D.; Yang, Y.; Huang, Z. Computational modelling of bone fracture healing under partial weight-bearing exercise. *Med. Eng. Phys.* **2017**, *42*, 65–72. [CrossRef]
9. Ganse, B.; Yang, P.F.; Gardlo, J.; Gauger, P.; Kriechbaumer, A.; Pape, H.C.; Koy, T.; Müller, L.P.; Rittweger, J. Partial weight bearing of the tibia. *Injury* **2016**, *47*, 1777–1782. [CrossRef]
10. Duda, G.N.; Bartmeyer, B.; Sporrer, S.; Taylor, W.R.; Raschke, M.; Haas, N.P. Does partial weight bearing unload a healing bone in external ring fixation? *Langenbecks Arch. Surg.* **2003**, *388*, 298–304. [CrossRef]
11. Ganse, B.; Orth, M.; Roland, M.; Diebels, S.; Motzki, P.; Seelecke, S.; Kirsch, S.M.; Welsch, F.; Andres, A.; Wickert, K.; et al. Concepts and clinical aspects of active implants for the treatment of bone fractures. *Acta Biomater.* **2022**, *146*, 1–9. [CrossRef] [PubMed]
12. Frost, H.M. Bone "mass" and the "mechanostat": A proposal. *Anat. Rec.* **1987**, *219*, 1–9. [CrossRef]
13. Chen, N.; Danalache, M.; Liang, C.; Alexander, D.; Umrath, F. Mechanosignaling in osteoporosis: When cells feel the force. *Int. J. Mol. Sci.* **2025**, *26*, 4007. [CrossRef]
14. Lacroix, D.; Prendergast, P.J. A mechano-regulation model for tissue differentiation during fracture healing: Analysis of gap size and loading. *J. Biomech.* **2002**, *35*, 1163–1171. [CrossRef]
15. Hasan, I. Computational Simulation of Trabecular Bone Distribution Around Dental Implants and the Influence of Abutment Design on the Bone Reaction for Implant-Supported Fixed Prosthesis. Ph.D. Thesis, University of Bonn, Bonn, Germany, 2011.
16. Claes, L.E.; Heigele, C.A.; Neidlinger-Wilke, C.; Kaspar, D.; Seidl, W.; Margevicius, K.J.; Augat, P. Effects of mechanical factors on the fracture healing process. *Clin. Orthop. Relat. Res.* **1998**, *355*, S132–S147. [CrossRef]
17. Jang, I.G.; Kim, I.Y.; Kwak, B.B. Analogy of strain energy density based bone-remodeling algorithm and structural topology optimization. *J. Biomech. Eng.* **2009**, *131*, 011012. [CrossRef] [PubMed]
18. Nayak, G.S.; Roland, M.; Wiese, B.; Hort, N.; Diebels, S. Influence of implant base material on secondary bone healing: An in silico study. *Comput. Methods Biomech. Biomed. Eng.* **2025**, *28*, 1734–1742. [CrossRef]
19. Checa, S.; Prendergast, P.J. A mechanobiological model for tissue differentiation that includes angiogenesis: A lattice-based modeling approach. *Ann. Biomed. Eng.* **2009**, *37*, 129–145. [CrossRef]
20. Shefelbine, S.J.; Augat, P.; Claes, L.; Simon, U. Trabecular bone fracture healing simulation with finite element analysis and fuzzy logic. *J. Biomech.* **2005**, *38*, 2440–2450. [CrossRef] [PubMed]
21. Nutu, E. Interpretation of parameters in strain energy density bone adaptation equation when applied to topology optimization of inert structures. *Mechanika* **2015**, *21*, 443–449. [CrossRef]
22. Celik, S. Simulation of Bone Remodeling Process Around Dental Implant During the Healing Period. Ph.D. Thesis, University of Bonn, Bonn, Germany, 2021. [CrossRef]
23. Frost, H.M. The Utah paradigm of skeletal physiology: An overview of its insights for bone, cartilage and collagenous tissue organs. *J. Bone Miner. Metab.* **2000**, *18*, 305–316. [CrossRef]
24. Lin, C.L.; Lin, Y.H.; Chang, S.H. Multi-factorial analysis of variables influencing the bone loss of an implant placed in the maxilla: Prediction using FEA and SED bone remodeling algorithm. *J. Biomech.* **2010**, *43*, 644–651. [CrossRef] [PubMed]
25. Li, J.; Li, H.; Shi, L.; Fok, A.S.L.; Ucer, C.; Devlin, H.; Horner, K.; Silikas, N. A mathematical model for simulating the bone remodeling process under mechanical stimulus. *Dent. Mater.* **2007**, *23*, 1073–1078. [CrossRef] [PubMed]
26. Carter, D.R. Mechanical loading histories and cortical bone remodeling. *Calcif. Tissue Int.* **1984**, *36*, S19–S24. [CrossRef] [PubMed]
27. Sharir, A.; Barak, M.M.; Shahar, R. Whole bone mechanics and mechanical testing. *Vet. J.* **2008**, *177*, 8–17. [CrossRef]
28. Choi, K.; Kuhn, J.L.; Ciarelli, M.J.; Goldstein, S.A. The elastic moduli of human subchondral, trabecular, and cortical bone tissue and the size-dependency of cortical bone modulus. *J. Biomech.* **1990**, *23*, 1103–1113. [CrossRef]
29. Holmes, D.C.; Loftus, J.T. Influence of bone quality on stress distribution for endosseous implants. *J. Oral Implantol.* **1997**, *23*, 104–111.
30. Orth, M.; Ganse, B.; Andres, A.; Wickert, K.; Warmerdam, E.; Müller, M.; Diebels, S.; Roland, M.; Pohlemann, T. Simulation-based prediction of bone healing and treatment recommendations for lower leg fractures: Effects of motion, weight-bearing and fibular mechanics. *Front. Bioeng. Biotechnol.* **2023**, *11*, 1067845. [CrossRef]

31. Bergmann, G.; Graichen, F.; Rohlmann, A. Hip joint contact forces during walking and running, measured in two patients. *J. Biomech.* **2001**, *34*, 859–871. [CrossRef]
32. Bergmann, G.; Damm, P. *OrthoLoad—Database of Orthopedic Joint Loads*; Charité: Berlin, Germany, 2008; Available online: http://www.orthoload.com (accessed on 1 August 2025).
33. Weinans, H.; Huiskes, R.; Grootenboer, H.J. The behavior of adaptive bone-remodeling simulation models. *J. Biomech.* **1992**, *25*, 1425–1441. [CrossRef]
34. Liu, C.; Carrera, R.; Flamini, V.; Kenny, L.; Cabahug-Zuckerman, P.; George, B.M.; Hunter, D.; Liu, B.; Singh, G.; Leucht, P.; et al. Effects of mechanical loading on cortical defect repair using a novel mechanobiological model of bone healing. *Bone* **2017**, *108*, 145–155. [CrossRef] [PubMed]
35. Gardner, M.J.; van der Meulen, M.C.H.; Demetrakopoulos, D.; Wright, T.M.; Myers, E.R.; Bostrom, M.P. In vivo cyclic axial compression affects bone healing in the mouse tibia. *J. Orthop. Res.* **2006**, *24*, 1679–1686. [CrossRef]
36. Mehta, M.; Strube, P.; Peters, A.; Perka, C.; Hutmacher, D.; Fratzl, P.; Duda, G.N. Influences of age and mechanical stability on volume, microstructure, and mineralization of the fracture callus during bone healing: Is osteoclast activity the key to age-related impaired healing? *Bone* **2010**, *47*, 219–228. [CrossRef]
37. Funk, J.R.; Rudd, R.W.; Kerrigan, J.R.; Crandall, J.R. The line of action in the tibia during axial compression of the leg. *J. Biomech.* **2007**, *40*, 2277–2282. [CrossRef]
38. Kemper, A.; McNally, C.; Kennedy, E.; Manoogian, S.; Duma, S. The material properties of human tibia cortical bone in tension and compression: Implications for the tibia index. In Proceedings of the 20th International Technical Conference on the Enhanced Safety of Vehicles, Lyon, France, 18–21 June 2007.
39. Claes, L.E.; Heigele, C.A. Magnitudes of local stress and strain along bony surfaces predict the course and type of fracture healing. *J. Biomech.* **1999**, *32*, 255–266. [CrossRef] [PubMed]
40. Yang, P.F.; Kriechbaumer, A.; Albracht, K.; Sanno, M.; Ganse, B.; Koy, T.; Shang, P.; Brüggemann, G.P.; Müller, L.P.; Rittweger, J. On the relationship between tibia torsional deformation and regional muscle contractions in habitual human exercises in vivo. *J. Biomech.* **2015**, *48*, 456–464. [CrossRef] [PubMed]
41. Yang, P.F.; Sanno, M.; Ganse, B.; Koy, T.; Brüggemann, G.P.; Müller, L.P.; Rittweger, J. Torsion and antero-posterior bending in the in vivo human tibia loading regimes during walking and running. *PLoS ONE* **2014**, *9*, e94525. [CrossRef]